Quantum computation with Majorana zero modes in superconducting circuits

Heck, B. van

Chapter 7

Realization of microwave quantum circuits using hybrid superconducting-semiconducting nanowire Josephson elements

In superconducting electronic circuits, macroscopic degrees of freedom like currents and voltages can exhibit quantum mechanical behavior. These circuits can be designed to behave as artificial atoms, having a discrete set of energy levels which can be driven coherently [30]. In the field of circuit quantum electrodynamics (cQED), these artificial atoms are coupled to resonators to perform microwave quantum optics in the solid state [165, 166]. Over the last decade, cQED has also grown into a promising platform for quantum information processing, wherein the ground and first-excited levels of each atom serve as an effective qubit [31]. To date, implementations of superconducting quantum circuits have relied almost exclusively on aluminum/aluminum-oxide/aluminum (Al/AlOx/Al) tunnel junctions as the source of non-linearity without dissipation. However, many exciting applications require magnetic fields (~ 0.5 T) at which superconductivity in aluminum is destroyed, calling for an alternative approach to realizing microwave artificial atoms.

Recent advances in materials development and nanowire (NW) growth have enabled the development of superconductor-semiconductor (super-semi) structures supporting coherent charge transport without dissipation [167], and providing signatures of Majorana bound states citemourik2012. To date, super-semi-super Josephson elements (JEs) have been studied exclusively in quasi-DC transport [168–171]. Building microwave circuits operating in the quantum regime, in which transition energies between levels exceed the thermal energy, offers news ways to investigate the physics of hybrid super-semi structures using spectroscopy [150, 151, 155].

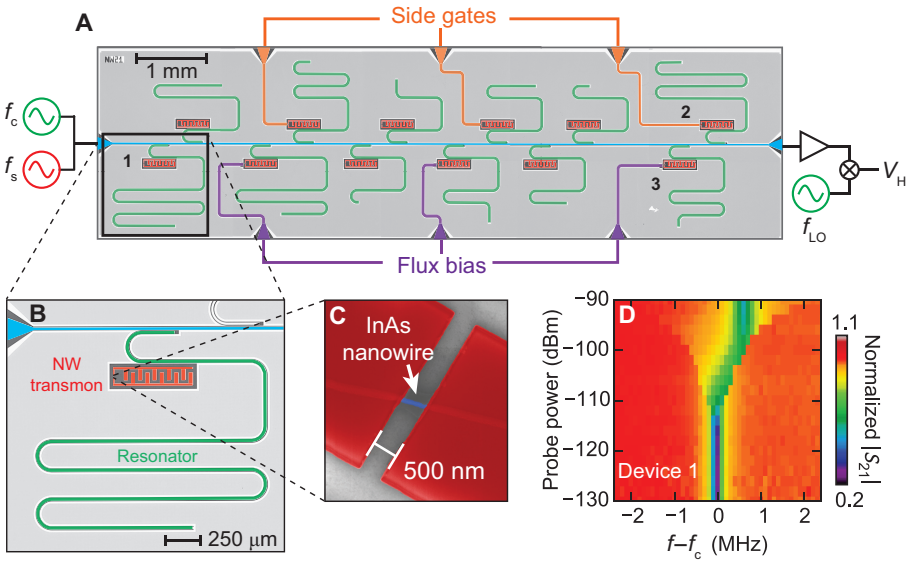

Figure 7.1: Hybrid Josephson elements in cQED. (**A**) Overview of cQED chip allowing control and readout of NW circuits using dedicated resonators (green) coupled to a common feedline (blue). For readout, a microwave tone with frequency f_c is applied near the fundamental of the resonator coupling to the NW circuit under study. The signal is amplified and down-converted to 1 MHz using a local oscillator at f_{LO} for subsequent digitization and processing. Additional controls on a subset of devices include side gates (orange) for electrostatic tuning of carrier density in the NW of single-junction devices, and short-circuited transmission lines (purple) for threading flux through the loops of split-junction devices. (**B**) Optical zoom-in of Device 1, containing a single-junction NW circuit (red). (**C**) Scanning electron microscope (SEM) image of an InAs NW (blue) contacted by NbTiN electrodes (red) separated by 500 nm. (**D**) Normalized feedline transmission as a function of readout power. The resonator shifts from $f_c = 3.9464$ GHz at single-photon level to $f_{bare} = 3.9470$ GHz above 10^5 photons. This shift confirms the coupling of the resonator to a non-linear circuit..

7.1 Description of the experimental setup

We report the realization of super-semi microwave circuits in cQED. Our chip (Fig. 7.1A) contains multiple capacitively shunted single and double NW JEs coupled to dedicated transmission-line resonators for control and readout using a common feedline (Fig. 7.1B). The chip contains side gates for electrostatic tuning of some single-junction devices and current-bias lines for threading flux through the loops of split-junction devices. We created each JE by deterministically placing an InAs NW between the leads

of a pre-patterned NbTiN interdigitated capacitor (IDC) and contacting the NW to each lead in a subsequent NbTiN deposition. The charging energy $E_C \approx h \times 300$ MHz of the devices is chosen much smaller than the estimated Josephson coupling energy E_J of the NW junction, as in conventional transmon devices [37], leading to a weakly anharmonic energy spectrum (energies E_i) of circuit plasma modes. We first verify the presence of the non-linear NW circuit by measuring the feedline transmission near the fundamental frequency of the coupled resonator (Fig. 7.1D). The Jaynes-Cummings interaction leads to different resonator frequencies f_c and f_{bare} at single- and many-photon probe levels, respectively [172, 173]. We then search for the qubit transition frequency f_{01} of the NW circuit by monitoring feedline transmission at f_c while sweeping a second tone [60] near the estimated frequency $f_{bare}+(f_{bare}-f_c)/g^2$, where g is the coupling strength between NW circuit and resonator.

7.2 Spectroscopy of single-junction devices

We first investigate the electric-field effect on the NW-circuit spectrum (Fig. 7.2A). Device 2 has one NW junction (measured length $L \approx 550$ nm) and a proximal side-gate electrode for tuning the carrier density in the NW. We observe fully reproducible fluctuations (see Appendix 7.B) in f_{01} as a function of the side-gate voltage V_g, indicating diffusive charge transport in the NW. Using the plasma-oscillation relation [37], $E_J \approx f_{01}^2/8E_C$, we determine the root-mean-square Josephson-energy fluctuation $\sqrt{\langle \delta^2 E_J \rangle}/h \approx 2$ GHz in the $V_g = 0-10$ V range. Matching this scale to the Thouless energy [174], $E_{Th} = \hbar D/L^2$, and assuming highly transparent contacts [170], we estimate the diffusion constant $D \approx 40$ cm^2/s. This value is typical for InAs wires [168].

Side-gate tuning of the NW junction offers a new means to control the spectrum of transmons. Decreasing V_g brings f_{01} into resonance with the resonator, revealing multiple avoided crossings (Fig. 7.2B). The minimum splitting indicates $g/2\pi = 34 \pm 1$ MHz (Fig. 7.2C). We note that while we only perform quasistatic field-effect tuning of f_{01} throughout this experiment, nanosecond control should be possible by increasing the bandwidth of off-chip filtering.

We now discuss the impact of charge fluctuations on the observed linewidth of the f_{01} transition, which is of interest for qubit applications. Transmon qubits are by design insensitive to charge offset fluctuations on the superconducting islands [37], owing to the exponential suppression of charge dispersion when $E_J \gg E_C$. Field-effect control of the Josephson coupling can make f_{01} sensitive to nearby fluctuating charges. One may expect a region with $\partial f_{01}/\partial V_g = 0$ to constitute a charge sweet-spot [175] and thus to correlate with a linewidth reduction. However, we do not observe a correlation between the linewidth $\gamma/2\pi > 10$ MHz and $\left|\partial f_{01}/\partial V_g\right|$, suggesting a different dominant decoherence channel (see Appendix 7.B). We surmise a connection between this broad linewidth and the soft gap induced in NWs contacted by NbTiN using similar fabrication techniques [74]. Parallel experiments by the Copenhagen group achieve hard induced gaps in epitaxial Al-InAs NWs [176] and ~ 1 μs coherence

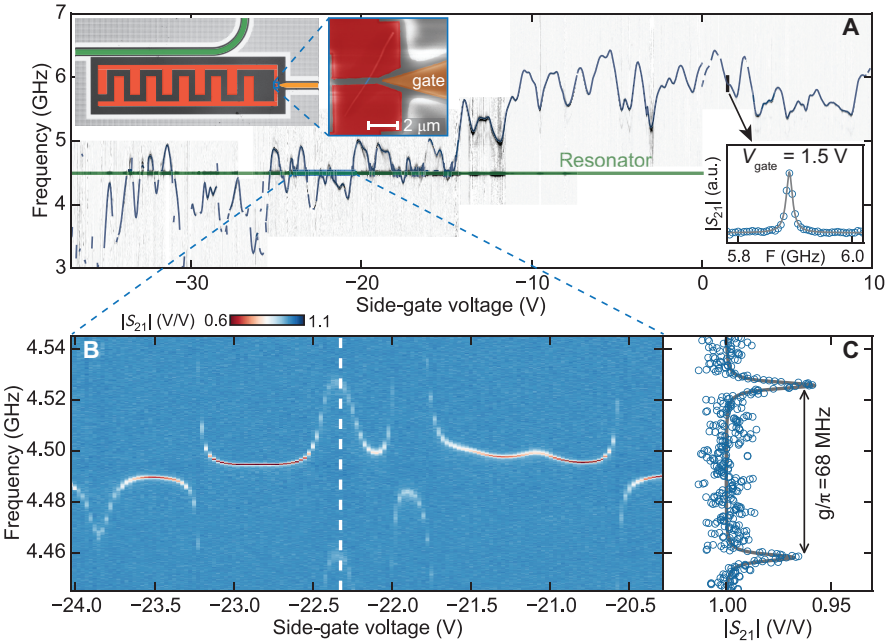

Figure 7.2: Side-gate tuning of a NW circuit and mesoscopic Josephson coupling fluctuations. (**A)** Left inset; false-colored optical image of Device 2. Right inset; SEM micrograph showing the single NW junction and the proximal side gate (orange) for voltage control. Sweeping this voltage induces reproducible fluctuations in the qubit transition frequency f_{01}. Lower inset; example spectroscopy of the qubit transition, showing an inhomogeneously broadened linewidth $\gamma/2\pi = 13.2 \pm 0.3$ MHz. A downward trend in f_{01} is observed as V_g decreases. At $V_g < -15$ V, f_{01} fluctuates around the resonator fundamental (green line). (**B**) A zoom-in around $V_g = -22$ V shows multiple avoided crossings. (**C**) At $V_g = -22.3$ V, the NW circuit fully hybridizes with the resonator. From the minimum splitting, we extract the NW circuit-resonator coupling strength $g/2\pi = 34 \pm 1$ MHz.

times in a single-JE hybrid transmon [177].

7.3 Spectroscopy of a double-junction device

Next, we consider a split-junction device where the two parallel JEs (each with $L = 150$ nm) are created from one 5 μm long NW (Fig. 7.3A). As in conventional transmons, f_{01} first decreases as flux Φ is threaded through the loop. However, near $\Phi \sim \Phi_0/2$ ($\Phi_0 = h/2e$ is the flux quantum), a clear departure from transmon-like

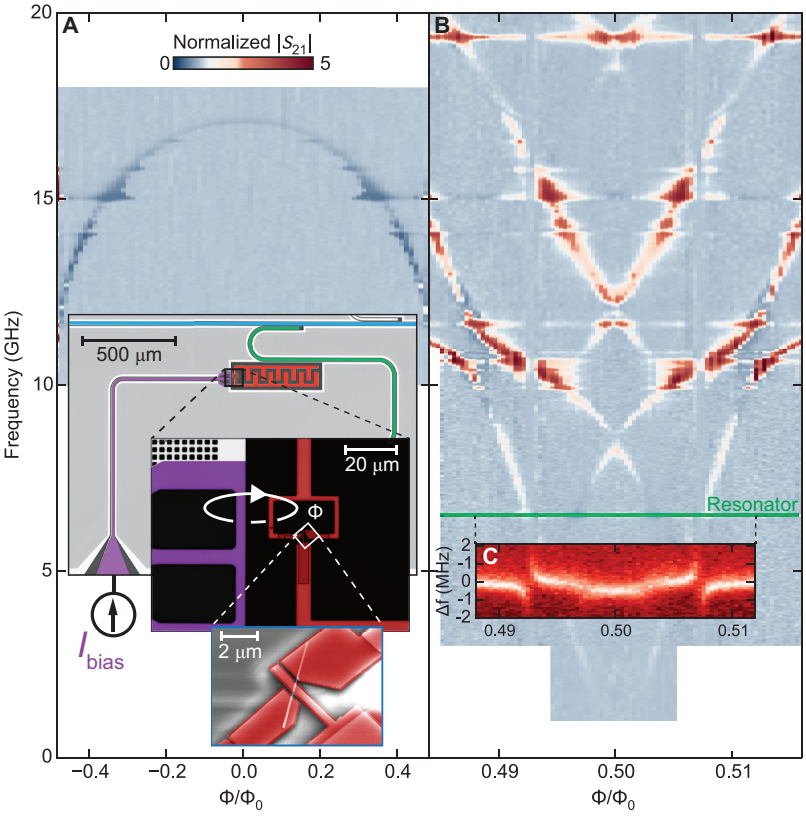

Figure 7.3: Flux bias spectroscopy of a split-junction NW circuit. (**A**) Inset: false-colored optical image showing Device 3 (red), its resonator (green), and flux-bias line (purple). Bottom inset: SEM micrograph of the two JEs made from one NW. Flux-bias spectroscopy shows the tuning of f_{01} with Φ. (**B**) A high-resolution sweep around $\Phi = \Phi_0/2$ shows a strong flux dependence of the NW circuit transitions. (**C**) Measurement of resonator transmission around f_c with same horizontal range as in (**B**). The avoided crossing of the lowest transition with the resonator reveals a much reduced coupling strength.

behavior is observed (Fig. 7.3B). Multiple strongly flux-dependent transitions and a new, strong avoided crossing appear symmetrically about $\Phi_0/2$. In addition, the avoided crossing between the lowest transition and the resonator is strongly reduced

(Fig. 7.3c) compared to that of Device 2 [1].

The observed deviation from the conventional transmon energy spectrum provides a signature of non-sinusoidal current-phase relations (CΦRs) in the NW junctions [178]. We now show that the observed spectrum can be fully explained by the Hamiltonian of a Cooper-pair box (CPB): $H = 4E_C\hat{N} + V_1(\hat{\delta}) + V_2(2\pi\Phi/\Phi_0 - \hat{\delta})$, provided its split junctions do not follow a cosine-shaped Josephson potential (Fig. 7.4A). Here, the operators $\hat{N}$ and $\hat{\delta}$ represent the charge imbalance between islands and the phase difference across NW junction 1, respectively. The Josephson potential $V_i(\varphi_i)$ of junction i is linked to its CΦR by $I_i(\varphi_i) = (2\pi/\Phi_0)\,\partial V_i/\partial\varphi_i$, where $\varphi_1 \equiv \hat{\delta}$ and $\varphi_2 \equiv 2\pi\Phi/\Phi_0 - \hat{\delta}$. Crucially, we require V_i to be 2π-periodic but not necessarily cosine shaped. Using a simple phenomenological model [174] of the form $V_i(\varphi_i) = -K_i\sqrt{1 - T_i\sin^2(\varphi_i/2)}$ and performing a non-linear least-squares fit with five free parameters, we obtain a quantitative match to all spectral data (best-fit values are $E_C/h = 279\pm1$ MHz, $K_1/h = 376\pm13$ GHz, $K_2/h = 233\pm2$ GHz, $T_1 = 0.86\pm0.02$, and $T_2 = 0.885 \pm 0.004$, see also Appendix 7.D). As shown in Fig. 7.4A, the corresponding CΦRs are evidently skewed. A three-parameter fit using V_i corresponding to the CΦR of a short, diffusive point contact in the many-channel limit [178, 179] showed only slightly worse agreement, as did a truncated Fourier series expansion of V_i. All approaches produce similar skewed CΦRs (see Appendix 7.D).

Interestingly, this device can be operated in two distinct regimes by tuning Φ. Near $\Phi = 0$, it operates like a transmon, whose eigenstates are plasma modes with a weakly anharmonic spectrum. Around $\Phi \simeq \Phi_0/2$, it operates like a flux qubit [180] whose two lowest energy levels carry opposite persistent currents $I_{p,i} = \partial E_i/\partial\Phi$, which we estimate to be of order ±100 nA (see Appendix 7.E). The possibility to drive transitions between these distinct persistent-current states using coherent microwaves constitutes a manifestation of macroscopic quantum coherence [181] in our NW circuits.

In conclusion, we have realized the first hybrid microwave circuits made from super-semi NW JEs and characterized them using spectroscopy. NW circuits offer several advantages over traditional aluminum circuits. First, tuning qubit transitions using the field effect in single NW JE devices offers an attractive alternative to flux biasing of split-junction Al devices. Second, these NW circuits are made exclusively from magnetic-field compatible materials. Magnetic-field compatible super-semi NW microwave circuits have the potential to open new avenues of research. In particular, very pure solid-state electron spin ensembles (e.g., nitrogen impurities in diamond or phosphorous donors in silicon) could be field-polarized to make coherent quantum memories [182, 183] for hybrid quantum processors. In addition, the microwave circuits realized here may be useful to control and readout Majorana bound states [21, 107] in proposed demonstrations of non-Abelian exchange statistics [6, 11, 14, 27]. Immediate next experiments will therefore focus on the study of these circuits in up

[1] Moreover, several flux-independent lines appear. We can attribute many of these to the fundamentals and higher harmonics of other resonators on the chip (they are also observed when we studied other devices on this chip) and are not considered henceforth.

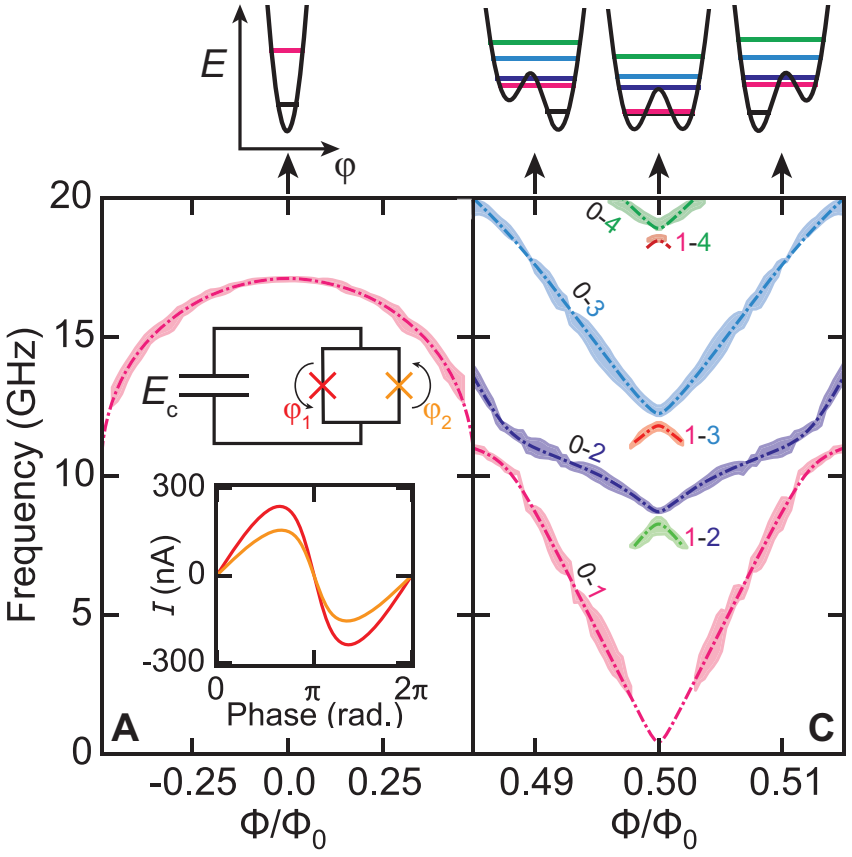

Figure 7.4: Fitting theory to the spectrum of the split-junction NW circuit. (**A**) Top inset; equivalent circuit of the device, a split Cooper-pair box containing a loop interrupted by two NW JEs (phase differences $\varphi_{1,2}$), threaded by an externally applied flux Φ, and shunted by a capacitance, giving total charging energy E_C. Around $\Phi = 0$, the Josephson potential has a single minimum, producing a weakly anharmonic spectrum. (**B**) The non-sinusoidal current-phase relation of the NW JEs determines the particular flux-dependence of the transition frequencies around $\Phi = \Phi_0/2$ as the Josephson potential develops a symmetric double-well profile that tilts as Φ is tuned away from $\Phi_0/2$. All curves are the result of a least-squares non-linear fit of the theoretical model described in the text. We identify four fundamental transitions from the ground state and three transitions from the first-excited state.

to ~ 0.5 T in-plane magnetic fields.

7.A Materials and Methods

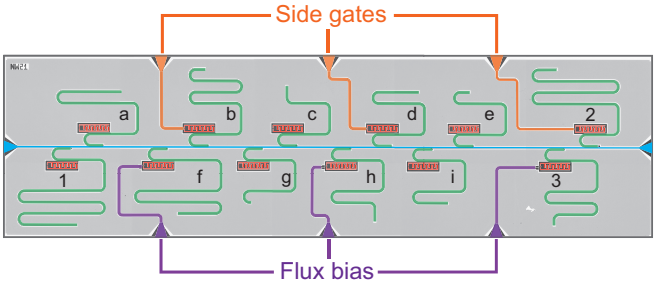

Figure 7.5: Overview of the chip.

Device	R_{RT} (kΩ)	L (nm)	f_c (GHz)	f_{01} (GHz)	Description
1	5.7	500	4	6.7	single
2	6.2	500	4.5	6.2 ($V_g = 0$ V)	single, with gate
3	2.2	200	6.5	17 (max)	split, with flux control
a	3.03	200	7	not < 20	single
b	3.07	200	6	13.6	single, with gate
c	short	50	11	-	single
d	open	100	8.5	-	single, with gate
e	short	50	10	-	single
f	3.5	500	5	9.1 (max)	split, with flux control
g	short	50	10.5	-	single
h	1.4	100	8	not < 20	split, with flux control
i	2.6	100	9	not < 20	single

Table 7.1: Overview of devices on the chip. R_{RT} is the two-terminal resistance probed close to the junction at room temperature. L indicates the design length.. The first three devices in the table are those discussed in the main text, in Figures 7.1, 7.2, and 7.3 respectively.

The chip was fabricated on a sapphire substrate (single-side polished, C-plane cut, 430 μm thickness). After cleaning the substrate in buffered HF, a NbTiN film (80 nm thickness) was sputtered. Ground planes, resonators and IDCs were defined by negative tone electron-beam lithography and reactive ion etching.

In the next step, InAs NWs of typical length $5-10$ μm and radius $50-100$ nm were controllably deposited using a micro-manipulator setup equipped with an optical

microscope. Detailed structural and DC transport characterization of the InAs NWs used in this experiment have been published in earlier reports [184].

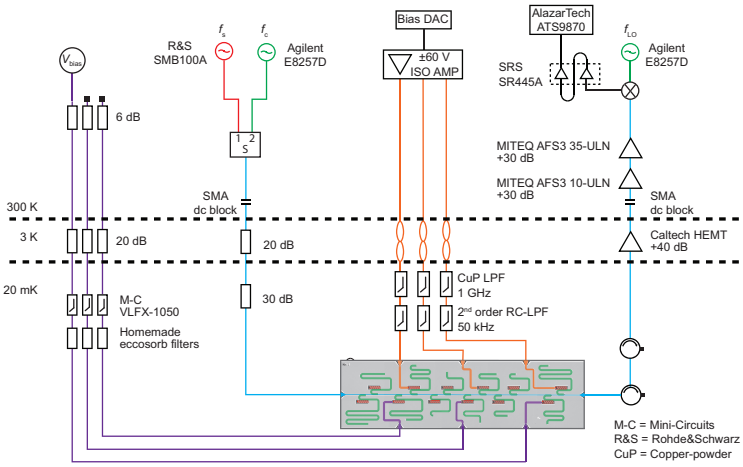

Figure 7.6: Wiring schematic of the experimental setup outside and inside the ^{3}He-^{4}He dilution refrigerator (Leiden Cryogenics CF-650). Readout (green) and spectroscopic (red) microwave drives are combined in a single coax line (blue) at room temperature. The line is attenuated at the 3 K and 20 mK stages before connecting to the chip feedline. The feedline output is isolated from the higher temperature stages by two circulators. The signal is amplified at the 3 K stage by a HEMT amplifier (Caltech Cryo1-12, 0.06 dB noise figure) and at room temperature by two Miteq amplifiers. The signal is down-converted to 1 MHz, further amplified, digitized and saved for processing. The setup contains wiring for gate (orange) and flux (purple) control on a subset of devices. Both types of control line are low-pass filtered.

The fine patterns were designed based on optical alignment to the NWs. The semiconductor-superconductor interface area was maximized by covering the NW as much as possible. The overlap between the coarse and the fine superconducting structures in each IDC was designed to be several tens of μm^2. After defining the fine pattern by positive tone electron-beam lithography, the semiconductor surface was cleaned in buffered HF for 20 s and then a 100 nm thick NbTiN film was sputtered in order to overlay the coarse structures as well.

In total, twelve devices were fabricated on the chip (Fig. 7.5), and each was coupled to a coplanar waveguide quarter-wave resonator with a distinct fundamental frequency in the range 4 to 11 GHz. Table 7.1 gives an overview of all the devices on the chip. Gate voltages in the range ±40 V were applied through on-chip 50 Ω transmission lines with open ends proximal to the NW. Off-chip, the lines are filtered by a second-order RC filter and a copper-powder (CuP) filter mounted to the mixing chamber plate of the refrigerator (Fig. 7.1). The two filters have $\sim$ 50 kHz and

$\sim$ 1 GHz cutoff frequencies, respectively. The JEs of split-junction devices were embedded in a superconducting loop of area $13 \times 24\ \mu\text{m}^2$. Flux through the loop is controlled using on-chip 50 Ω transmission lines, with short-circuited termination proximal to the loop. Off-chip, the lines are low-pass filtered with nominal 1 GHz cutoff frequency.

7.B Additional data for Device 2

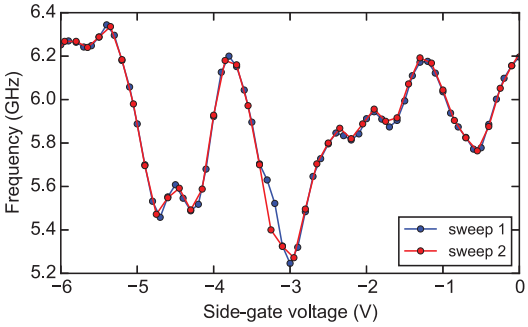

Figure 7.7: Reproducibility of the f_{01} fluctuations. Two sweeps of two-tone spectroscopy show the reproducibility of the f_{01} fluctuations. These sweeps were separated by two days.

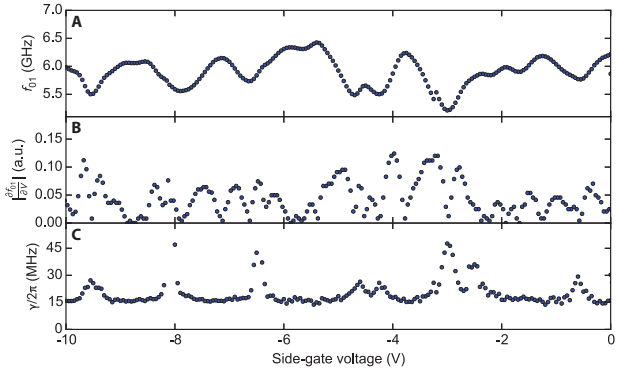

Figure 7.8: Absence of correlation between f_{01} field-effect sensitivity and linewidth γ. **(A)** Qubit transition frequency f_{01} as a function of V_g, extracted from Fig. 7.2. **(B)** Computed field-effect sensitivity $\left|\partial f_{01}/\partial V_g\right|$. **(C)** Extracted γ. Vanishing $\left|\partial f_{01}/\partial V_g\right|$ does not correlate with a reduction in γ.

7.C Data extraction from flux-bias spectroscopy

In order to perform fits to the observed spectroscopy lines, we have extracted a set of data points with error bars from the raw data, consisting of a 2D scan of feedline transmission measured as a function of frequency f and voltage V_{bias} applied to the 50 Ω bias line. We used the following procedure to extract the points [2].

1. We applied a Gaussian filter to suppress noise fluctuations, and subtracted the residual background signal.

2. We converted V_{bias} into flux Φ through the loop, assuming a linear relation $\Phi = AV_{\text{bias}} + B$.

3. We identified isolated features in the raw data by removing all points below a transmission threshold. Every isolated feature consisted of a connected set of data points surrounding peaks of high transmission in the f-Φ plane.

4. Within every feature, we extract a single data point for each voltage value. The frequency f and uncertainty Δf of every point was computed by taking the average frequency of all points in the same feature with the same V, weighted by their transmission amplitude. This procedure provided a collection of data points $(\Phi, f, \Delta f)$. The points were manually divided into groups forming continuous $f(\Phi)$ transition lines.

7.D Theoretical model and fits for Device 3

Many features of the observed transitions coincide with those expected for a double-well potential. The first is the linear vanishing of f_{01} at $\Phi = \Phi_0/2$, which is consistent with the small energy difference between the ground and first-excited states in a symmetric double-well potential. The second is the appearance of a strong avoided crossing between the two lowest transitions at $\Phi \simeq 0.49\Phi_0$. The avoided crossing naturally arises in a tilted double-well potential, when the lowest energy state in the shallower well becomes resonant with the first-excited state of the deeper well. The third is the visibility of transitions whose frequency decreases away from $\Phi = \Phi_0/2$, which is consistent with residual thermal population of the first-excited state close to $\Phi_0/2$.

The transition frequencies obtained from the energy levels of the split-junction CPB Hamiltonian,

$$H = 4E_{\text{C}}\hat{N} + V_1(\hat{\delta}) + V_2(2\pi\Phi/\Phi_0 - \hat{\delta}). \tag{7.1}$$

were fit to the extracted data points. The energy levels were computed numerically in the eigenbasis of the charge operator $\hat{N}$, truncating the Hilbert space to ~ 200 states

[2] A dynamic IPython Notebook containing the relevant code and illustrating the data extraction process is available online at the page http://goo.gl/3xfGr8.

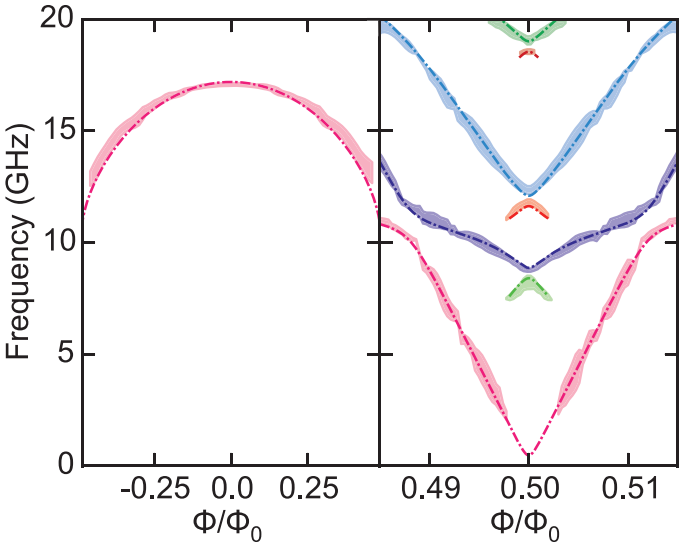

Figure 7.9: Fit to the K-O model. Best-fit values are $E_C/h = 266 \pm 2$ MHz, $K_1/h = 218 \pm 1$ GHz, and $K_2/h = 141 \pm 1$ GHz.

such that convergence was reached. Via a Fourier series expansion of the 2π-periodic functions

$$V_i(\varphi_i) = -\sum_n A_{i,n} \cos(n\,\varphi_i), \tag{7.2}$$

the Josephson terms in the Hamiltonian can be easily expressed in the same basis using the raising and lowering operators $\hat{N}_\pm = \exp(\pm i\hat{\delta})$,

$$\begin{aligned} V_1(\hat{\delta}) &= -\sum_n A_{1,n}(\hat{N}_+ + \text{h.c.}), \\ V_2(2\pi\Phi/\Phi_0 - \hat{\delta}) &= -\sum_n A_{2,n}(\hat{N}_+ e^{-i2\pi\Phi/\Phi_0} + \text{h.c.}). \end{aligned}$$

Hence, the Fourier series of V_i contains higher harmonics with period $2\pi/n$, with $n > 1$, allowing the total Josephson energy $V_1 + V_2$ to develop several local minima in a 2π interval, thereby forming a double-well potential. This situation is particularly relevant at $\Phi \simeq \Phi_0/2$, where the odd harmonics of V_1 and V_2 subtract. Time-reversal symmetry makes the minima degenerate at $\Phi = \Phi_0/2$ (Fig. 7.4).

Lacking exact knowledge of the CΦR of the junctions, we have tried different phenomenological models for the $V_i(\varphi_i)$:

1. The model presented in the text,

$$V_i(\varphi_i) = -K_i\sqrt{1 - T_i \sin^2(\varphi_i/2)}, \tag{7.3}$$

is strictly valid only for short junctions, with total amplitude $K_i \simeq n_i \Delta_0$, with Δ_0 the induced gap in the NW, resulting from n_i transport channels with a typical transparency T_i. This model leads to a Hamiltonian with five free parameters: E_C, K_1, K_2, T_1, and T_2. For the fit we took the Fourier series expansion of V_i and truncated to seven harmonics in the numerical diagonalization of the Hamiltonian.

2. The Kulik-Omelyanchuk (K-O) model for the zero-temperature current-phase relation of a diffusive and short point contact [178, 179] gives

$$V_i(\varphi_i) = -2K_i \int_0^{\pi/2} \sqrt{1 - \sin^2(\varphi_i/2)\sin^2 x}\, \mathrm{d}x. \tag{7.4}$$

The above relation can be obtained from Eq. (3) by integrating over the probability distribution of transmission coefficients T in a diffusive point contact. This model leads to a Hamiltonian with three free parameters, E_C, K_1, and K_2. As before, the Fourier series was truncated to seven harmonics. The best-fit results are shown in Fig. 7.9.

3. We have also performed a direct fit of the Fourier coefficients $A_{i,n}$, increasing the number of coefficients until a good agreement with the data was observed. The fit is more sensitive to the Fourier coefficients of the weak junction, as the asymmetry in junction strength makes the phase difference across the strong junction stay close to zero at any Φ. The best-fit values of the seven-parameter fit are $E_C/h = 275 \pm 1$ MHz, $A_{1,1}/h = 95.5 \pm 0.4$ GHz, $A_{2,1}/h = 68.9 \pm 0.2$ GHz, $A_{2,2}/h = -11.78 \pm 0.06$ GHz, $A_{2,3}/h = 3.28 \pm 0.02$ GHz, $A_{2,4}/h = -0.98 \pm 0.03$ GHz, and $A_{2,5}/h = 0.21 \pm 0.03$ GHz. Including more Fourier coefficients did not improve the agreement with the data, and increased the variance of the best-fit values.

Due to the non-linearity of the fitting model and correlated errors in the extracted data points, it is not straightforward to extract a figure of merit for quantitative comparison of the models. All models require at least one non-sinusoidal CΦR to fully explain all the features of the data set.

Although the data are well fit by non-sinusoidal CΦRs, there are other mechanisms that can produce similar spectra in superconducting circuits. First, the presence of a super-inductance is known to produce a potential landscape with several minima, as for the fluxonium [185]. NbTiN is known for its high kinetic inductance L_k. Indeed, in our circuit we estimate $L_k \approx 0.2$ nH and loop geometric inductance $L_{geo} \approx 30$ pH. The associated total inductive energy $E_L = (\Phi_0/2\pi)^2/L_k \approx h \times 800$ GHz is, however, much larger than $E_J \approx (K_1 T_1 + K_2 T_2)/4 = h \times 132$ GHz and therefore cannot produce multiple minima (fluxonium requires $E_L < E_J$). Second, microwave-induced excitation of Andreev bound states (ABS) confined to the junction can also produce a qualitatively similar spectrum [186]. However, ABS transitions below 2 GHz require almost perfectly transparent transport channels, which has proven

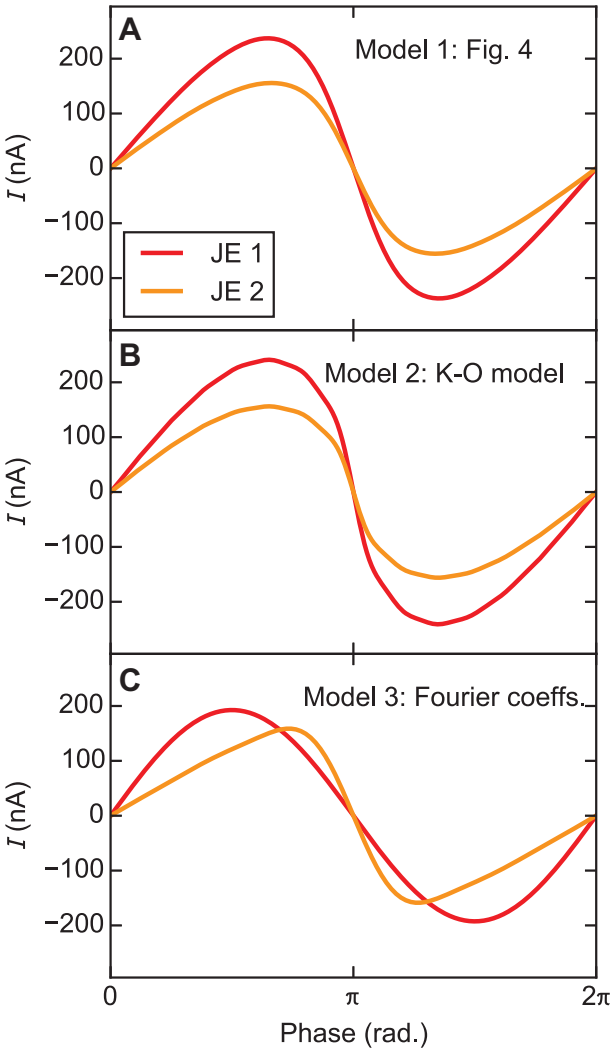

Figure 7.10: CΦRs for the three models. **(A)** Phenomenological model used in the main text. **(B)** K-O model. **(C)** Fourier series using one harmonic for JE 1 and five harmonics for JE 2.

challenging in even the most ideal atomic point contacts [186]. We therefore surmise that the JEs remain in their ABS ground state and that the observed spectrum is fully due to plasma modes. The potential to observe ABS transitions provides an exciting prospect for future work.

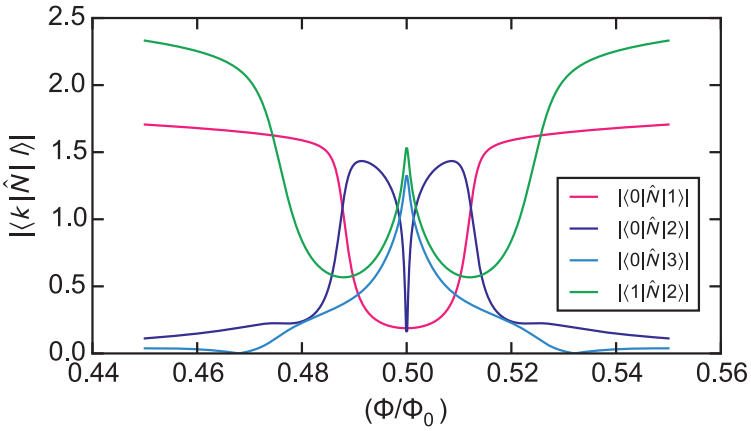

Figure 7.11: Flux-bias dependence of the NW-circuit-resonator coupling matrix elements for Device 3. The absolute matrix element $\left|\langle k|\hat{N}|l\rangle\right|$ determines the visibility of the transitions in Fig. 7.3 of the main text. As expected for transmons, only the matrix elements $\left|\langle k|\hat{N}|k+1\rangle\right|$ remain strong away from $\Phi = \Phi_0/2$.

7.E Estimation of Device 3 parameters from model

It is possible to estimate interesting properties of Device 3 using the best-fit model values presented in the main text. In particular, we can compute the dipolar couplings of the NW circuit to its resonator. The coupling strength of the dipole-induced transition between two eigenstates $|k\rangle$ and $|l\rangle$ of the split-junction CPB Hamiltonian is proportional to the corresponding matrix element of $\hat{N}$, $n_{kl} = \langle k|\hat{N}|l\rangle$.

Fig. 7.11 shows the calculated relative couplings $|n_{01}|$, $|n_{02}|$, $|n_{03}|$, and $|n_{12}|$ near $\Phi = \Phi_0/2$. Their flux dependence explains some interesting features of the data, in particular:

1. The vanishing visibility of the $0 \to 2$ transition at $\Phi = \Phi_0/2$.
2. The strong visibility of the $0 \to 3$ transition near $\Phi = \Phi_0/2$.
3. The reduction of $|n_{01}|$ near $\Phi_0/2$ (see Fig. 7.3) compared to that of Device 2.

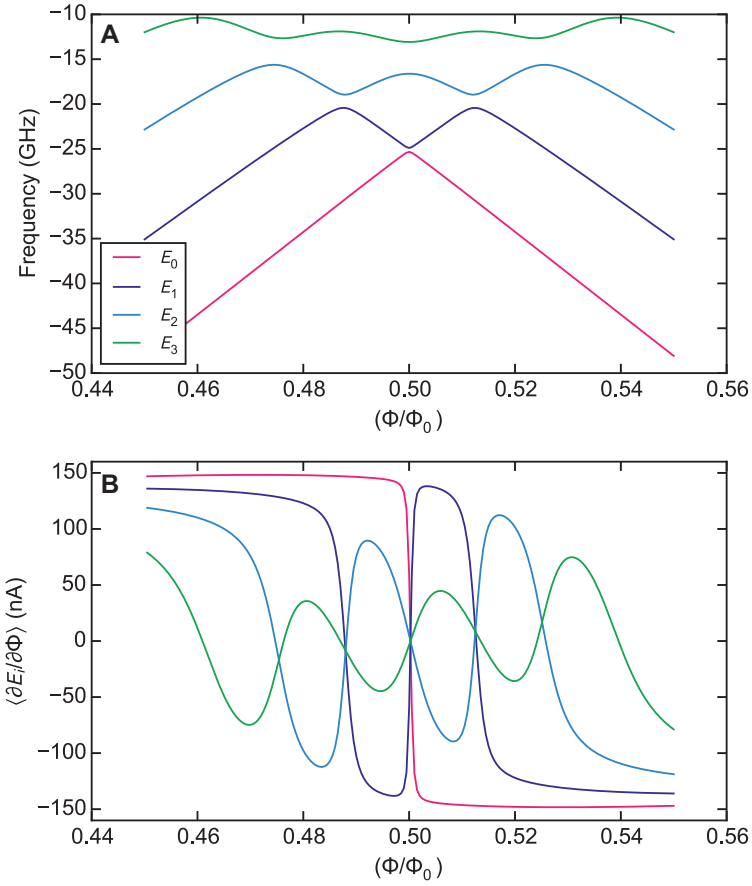

Figure 7.12: Energy levels of the split-junction NW circuit around $\Phi_0/2$. **(A)** Calculated energy levels for the parameters of Fig. 7.4 of the main text. **(B)** The states belonging to the lowest energy levels, E_0 and E_1, carry opposite persistent currents $I_{\mathrm{p},i} = \partial E_i/\partial \Phi$. The two states hybridize at $\Phi = \Phi_0/2$. Driving f_{01} with microwaves induces transitions between these two macroscopically distinct current states.